# Effect of Tensile Stress on the Passivity Breakdown and Repassivation of AISI 304 Stainless Steel: A Scanning Kelvin Probe and Scanning Electrochemical Microscopy Study

A. Nazarov, Vincent Vivier, F. Vucko, Dominique Thierry

# Effect of Tensile Stress on the Passivity Breakdown and Repassivation of AISI 304 Stainless Steel: a Scanning Kelvin Probe and Scanning Electrochemical Microscopy Study.

A. Nazarov[1z], V. Vivier[2], F. Vucko[1], D. Thierry[1]

[1] French Corrosion Institute, Brest, France
[2] Sorbonne Université, CNRS, Laboratoire Interfaces et Systèmes Electrochimiques, LISE, Paris, France
[Z] Corresponding author E-mail address: [andrej.nazarov@institut-corrosion.fr]

## Abstract

The interplay between mechanical stresses and electrochemical reactions may lead to stress corrosion cracking or hydrogen embrittlement for many materials. In this work, the effect of the tensile stress on the electrochemical properties of AISI 304 stainless steel was studied using scanning Kelvin probe (SKP) in air and scanning electrochemical microscopy (SECM) in an aqueous 0.5 M $Na_2SO_4$ electrolyte. The measurements were performed under load- and load-free conditions.

No influence of the elastic stress on the electrochemical potential of the steel was found. In contrast, the plastic strain induces dislocations and dislocation pile-ups, which emerge to the surface. The formation of new active surfaces is accompanied by an increase in the roughness and a 150-200 mV decrease in the steel potential. After activation, the potential increased due to passivation of the emerging surfaces by a newly grown oxide film, which took place under both the load and load-free conditions and followed a time dependence of $\boldsymbol{\varphi} = A \log t + B$. Formation and then passivation of the new surfaces increased and then decreased the reduction current of the mediator in the SECM measurements. The effect of residual stress stored in the steel due to the development of dislocations on the reactivity of the re-passivated surface was investigated.

*Keywords*: Scanning Kelvin probe, Scanning electrochemical microscopy, Stainless Steel, Passivity breakdown, Tensile stress.

## 1. Introduction

The passivity and stability of passive oxide films play important roles in the susceptibility of stainless steels to local corrosion phenomena such as pitting and stress corrosion cracking (SCC). The breakdown of the passive film by either mechanical or chemical factors is one of the important issues in the theory and understanding of SCC. According to the slip–dissolution model, cracks develop due to cycling processes resulting in successive active film rupture and dissolution and film repassivation processes. The film rupturing occurs due to the application of tensile stress generated by mechanical loading of the bulk of the material [1]. In addition, breakdown of the passive film can result from the migration of dislocations and dislocation pile-ups to the metal surface [2]. The strain rate and the surface repassivation rate inside the crack are key factors in the propagation of SCC [3-6]. Metallic structures are often working under an elastic stress load. The impact of elastic stress and plastic deformation on electrochemical properties is worth studying in detail.

Plastic deformation significantly increases the anodic dissolution rates of many metals when compared with the influence of elastic deformation [7]. The dissolution rate shows a marked rise at the beginning of the plastic region, whereas an increase in sample elongation leads to an asymptotic value for the dissolution rate. Plastic deformation increases the surface roughness and creates slip edges and dislocations, which contributed to and accelerate the anodic dissolution of the metal [7]. The effect of yielding on the anodic dissolution has been observed for stainless steel and was explained by Gutman using a thermodynamic approach [8, 9]. Selective slip dissolution is the result of a local excess in the Gibbs potential of an elastic stress field at the dislocation and slip bands [9]. Additionally, Sahal et al. [10] and Saito and Kuniya [11] showed that the dissolution rate of Ni in an acidic electrolyte is proportional to the dislocation density created by the plastic strain. Thus, the surface roughness associated with the emergence of slip bands accelerated the dissolution process [12].

Surface passivation is a competitive process for mechanical activation in the stress field. To describe the kinetics of passivation, scratched or abraded electrodes of different types of steel have been used in aqueous electrolytes following a technique developed by Burstein [13]. After mechanical removal of the surface oxide, rapid repassivation can be observed with currents reaching 10 A/cm$^2$ for AISI 304 steel. The rate of film growth has been shown to be controlled by a high-field ion conduction mechanism. For stainless steel, the first step of oxide film formation is oxygen adsorption. Thickening then occurs by migration of metal cations, oxide anions, or their vacancies under the influence of an electric field [14]. Thus, according to the field assisted ion migration theory, film growth is limited by ion migration, which is driven by the electric field in the oxide, and the growth of the film decreases the electric field, thus reducing the growth rate. Normally, the repassivation kinetics of AISI 304 austenitic steel follow the relation $i = K \cdot t^b$. Here, b characterizes the ability of the surface to passivate [14], and the thickness of an oxide film (L) can be obtained through integration of the current decay during passivation at a fixed potential according to equation 1:

$$L = A \log(t) + const. \quad \text{Eq. 1}$$

On the other hand, the Cabrera–Mott theory for the growth of a passive film predicts that the inverse of the oxide thickness varies logarithmically with time, as given in equation 2 [15]:

$$1/L = B \log(t) + const. \quad \text{Eq. 2,}$$

where A and B are constants and t is the time of passivation.

Plastic deformation of stainless steel may modify the passive oxide film [16-20] and the alloy bulk [21-24]. It has even been shown that elastic deformation due to local microplasticity can produce microcracks in the passive film and accelerate dissolution [16]. Plastic deformation of austenitic stainless steels leads to the formation of α-martensite, which decreases the ability of the steel to passivate [21-23]. Martensite has been found in deformed areas, where slip planes had intercepted the passive film and a large number of dislocations were concentrated. A less protective passive film is the result of cold work, which has been attributed to the presence of defects such as dislocation pile–ups at the grain boundaries [21]. From the point of view of Y. Boudinar et al., steel hardening, residual back stress, dislocations and slip bands enhance the surface reactivity and kinetics of anodic dissolution [24].

The properties of stressed surfaces have been investigated using classical electrochemical techniques, such as measurement of the open circuit potential (OCP), DC polarization techniques and electrochemical impedance spectroscopy (EIS). Normally, tensile deformation

decreases OCP and the modulus of the impedance of steel. However, the data obtained using these global measurements were averaged over the entire surface area exposed to the electrolyte, which makes difficult to associate any variations in the results to breaks in the oxide film, pitting formation, and the emergence of dislocation or slip bands. However, local electrochemical microprobe techniques can be used to correlate the surface heterogeneities (phases, grains, inclusions, etc.) to the electrochemical processes at the microscale. Thus, local electrochemical impedance spectroscopy (LEIS) [25], scanning electrochemical microscopy (SECM) [26-28], and scanning Kelvin probe (SKP) [25, 29, 30] provide efficient ways to characterize the surface reactivity due to plastic deformation. Using SECM in the electrolyte, it has been found that the rate of electron transfer from the steel surface (oxide film) to a molecule of the redox mediator decreased with increasing of strain [26]. This unusual result indicated the inhibiting influence of the tensile strain on the rates of electrochemical processes. However, this effect was also in line with an SECM study [27] that showed elastic stress applied to stainless steel electrodes slightly decreased the surface electrochemical activity. Conversely, an SECM study of a notched sample [28] noted that residual plastic stress increased the electrochemical activity. Thus, SECM studies have shown conflicting results regarding the effect of stress on the reactivity of a stainless steel surface. SKP mapping of the Volta potential in air has been useful for finding the electrochemical heterogeneity above stressed stainless steel electrodes [25, 29, 30]. Thus, the application of the tensile and compressive stresses locally decreased the Volta potential of 301LN austenitic steel because the plastic deformation creates dislocations and dislocation slips that break down the oxide film.

Thus, only a small number of studies have used local electrochemical techniques to study stressed steel surfaces, whereas these surfaces play significant roles in phenomena such as stress corrosion cracking. The present study reports the effect of tensile stress on the electrochemical properties of AISI 304 steel surfaces. SKP and SECM were applied to study the electrodes either in air or in electrolytic environments. The potential variations in air due to stress constraints were compared with open circuit potential (OCP) transients measured in a non-aggressive aqueous $Na_2SO_4$ electrolyte. The potential measurements provide information regarding the steel passivation and possible electrochemical reactions occurring at specific locations. SECM allowed us to determine the rate of electron transfer and the local reactivity of the strained surface in an aqueous electrolyte. X-ray photoelectron spectroscopy (XPS) was employed to characterize the effect of stress on the composition of the oxide film.

## 2. Experimental

### *2.1 Materials and mechanical properties of the samples*

The composition of the AISI 304Lstainless steel used in this study is reported in Table 1. The initial grain sizes were in the range of 10-20 μm. A thermomechanical treatment was used to increase the grain sizes to the range of 50 to 80 μm, and the final microstructure of the surface is shown in Figure 1. For this, the samples were tensile pre-strained at 30%, heated at 1030°C for 20 min under argon gas flux and cooled in air. Prior to the heat treatment, the samples were mechanically ground with 4000 grit SiC paper. After the heat treatment, grinding was used to remove the oxide layer. Finally, fine polishing was performed using 1 μm diamond paste. The samples were degreased in ethanol, rinsed in deionized water and stored in dry air. It was previously found [29] that the potential of steel significantly depends on the conditions of the oxide film. To obtain more uniform surface oxide films, the samples were heat treated at 100°C for 1 h.

Tensile samples were prepared from a 0.5 mm thick plate that was machined to obtain samples compatible with both the local probe techniques used and the *in situ* tensile setup. A schematic representation of the samples is shown in Figure 2. This specific shape was selected to obtain stress/strain gradient in the diminution area of the sample. The initial gauge length of the specimen was 10 mm. Local measurements were performed over the gauge section of the sample, which is the location with the maximum stress and strain, and over the surrounding diminution areas of the sample. The mechanical properties were determined by tensile testing of flat samples (Figure 2. a) with a strain rate of 0.0067 $s^{-1}$ using a hydraulic tensile testing machine (HC25 from Zwick). Figure 2. b shows a representative stress-strain-load relationship for a sample. The yield strength (YS) was evaluated at 300 MPa, corresponding to 1.5 kN. The ultimate tensile strength (UTS) was 650 MPa with an experimental load of 3.25 kN. The elongation to failure was in the range of 46-48%.

To evaluate the local plastic strain and stress, calculations were performed by finite elements modeling with ABAQUS software using the tensile properties of the steel. An example of a local strain distribution in a tensile sample for an imposed total displacement of 6 mm is shown in Figure 2. c. In this figure, the indicated values of 12.1 and 43 mm are set to show the spreading of the plastic deformation over the gauge section of the specimen, which was initially 10 mm long. Indeed, some non-negligible plastic deformation was found up to 21.5 mm from the center of the specimen. The deformation in the gauge section was approximately 27% in this case corresponding to a plastic of 0.267. Based on these simulations, the extent of the plastic strain over the sample can be estimated. To compare the experimental data and simulation results, the total elongation of the tensile sample and the applied load were used as entry data for simulations.

To apply the load during the SKP and SECM measurements, a constant load cell was used. After mounting the sample on the setup, a load gauge was installed either in the SKP chamber or on the moving table of the SECM instrument. A detailed description of the setup has previously been reported [25, 29]. A load gauge and “Mitutoyo” digital caliper were used to control the load and elongation, respectively.

### *2.2 Scanning Kelvin probe*

SKP is a non–invasive technique that measures the contact potential difference between a working electrode (*i.e.*, the AISI 304) and a vibrating reference electrode (CrNi alloy needle). In air, the two surfaces are separated to create a capacitor in which, due to the vibration and the variation of the distance, an *AC* current is generated. The current amplitude is proportional to the contact potential difference between the two electrodes. The potential of the probe is calibrated, which makes it possible to determine the potential of the working electrode relative to that of the reference. Thus, SKP is able to either determine the surface distribution of the Volta potential or monitor the Volta potential at a single point above the surface. Details and the theory of SKP can be found in the literature [31].
In this study, a height–controlled SKP instrument from Wicinski & Wicinski GbR was used. The reference electrode was a needle with a tip diameter of 100 µm, and the distance to the working electrode surface was approximately 50 µm. Surface contour mapping (topographic profile) was performed simultaneously with the potential mapping. Prior to the measurement, the potential of the probe was calibrated relative to that of a $Cu/CuSO_4$ electrode, but all potentials are given versus the standard hydrogen electrode (SHE). The measurements were performed in ambient air at 50-60% RH.

SKP measures the Volta potential that, after calibration using a reference reversible electrode, corresponds to the electrochemical potential [31, 32]. In dry air conditions, the measurement relates to the potential of steel in the passive state. The potential is controlled by the redox potential of the surface species [31]. In air, the steel is covered by an oxide film, maintaining passive conditions. The thickness of the oxide film influences the Volta potential [29]. The formation or failure of the passive film significantly changes the steel potential as measured by SKP [29]. We can expect SKP to measure the potential drop ($X_w$) across the oxide film and in the Helmholtz layer of the molecules adsorbed from the air (Eq. 3).

$$X_w = \frac{\mu_{ox} - \mu_e}{e} + F_b + \beta_{ox/air} \qquad \text{(Eq.3)}$$

The first term is the contact potential difference between the bulk alloy and oxide film, which relates to the difference in the corresponding Fermi levels of the electrons in the metal ($\mu_e$) and in the oxide ($\mu_{ox}$), *e*- is the elementary charge. The second potential drop ($F_b$) relates to the adsorption of environmental components (molecules of oxygen, water, etc.), which alters the conduction and valence bands in the semiconducting oxide film. The electric charges in the oxide are compensated for by the charges of the adsorbed species (e.g., $O_2^-$ ions), creating a potential drop ($\beta_{ox/air}$).

### *2.3 Scanning electrochemical microscopy (SECM)*

SECM was used to measure the effect of stress on the local electrochemical reactivity of the steel surface in an aqueous electrolyte (0.5 M $Na_2SO_4$) in the presence of a redox mediator (either 10 mM $K_3(Fe(CN)_6)$ or 1 mM ferrocene methanol). The measurements were performed in a 4-electrode electrochemical cell (using a Pt-grid counter electrode and a saturated calomel reference electrode). The cell was attached to the surface of the gauge section of the tensile sample using O-rings. The area of the sample exposed to the electrolyte was 0.35 $cm^2$, and the volume of the aqueous electrolyte in the cell was approximately 10 $cm^3$.

The radius of the platinum microelectrode was 12.5 µm. SECM approach curves were performed to position the Pt microelectrode at a controlled distance from the sample. The electrolyte resistance was simultaneously monitored with the local current. As such, the current variation gives information about the surface reactivity whereas the electrolyte resistance gives information about the topography. The size of the scanned area was 500 x 500 $\mu m^2$ at a scan rate of 10 µm/s. This value was selected as a tradeoff value between the experiment duration (about 40 min. per map) and minimizing the risk of crashing the tip into the working electrode surface. All the experiments were performed at least 2 or 3 times at different locations above the sample.

### *2.4 XPS analysis*

X-ray photoelectron spectrometry (XPS, Kratos Axis Ultra DLD) was used to investigate the effect of plastic strain on the passive layer of 304L stainless steel. Specific samples were prepared from 20 mm width and 0.5 mm thick strips. An unstrained reference sample and a sample strained at 20% plastic deformation were investigated using angular analysis at 0°, 30° and 60°. High-resolution spectra were obtained for the Fe, Cr, O and C elements. From the relative intensities of the Cr and Fe oxides and their corresponding metallic peaks, the thickness of the passive layer was evaluated by considering a bilayer, with a $Cr_2O_3$ inner layer and a $Fe_2O_3$ outer layer. Physical data were obtained from the literature [33]. The

spectrum of the O element was de-convoluted to evaluate the relative amounts of -$O_2$, -OH and $H_2O$ bonding.

### *2.5 3D Optical profiling for surface topography visualization*

Plastic deformation creates dislocations and dislocation pile-ups. To evaluate the effect of stress on the surface roughness, a light profiler (Veeco/Wyko NT1100) was used. The technique is based on using light interferometry to obtain high-resolution 3D surface images.

## 3. Experimental Results

### *3.1 Effect of tensile stress on the potential of 304 stainless steel.*

SKP was used to find the effect of stress on the electrochemical potential of steel at the center of the specimen including the gauge section and the surrounding area of the tensile sample as shown in Figure 2.a. The initial potential distribution across the gauge section was constant at ca. 370 ±5 mV vs. SHE. Figure 3 shows the distribution of the potential after application of a 350 MPa tensile load, corresponding to approximately 3% of deformation in the gauge section. As shown in the stress-strain dependence graph (Figure 2.b), this load corresponds to the beginning of the plastic deformation range. The stress decreases the potential at all measured areas (corresponding to a length of 30 mm). However, at the center of the gauge section, the potential was more negative than at the other measurement locations, which is in good agreement with the stress distribution model depicted in Figure 2.c. When the sample was exposed to the load for 5 h, the potential at all points along the sample increased by 20 mV (Figure 3.b). However, removing the load and performing the potential measurement at the rest does not change the potential profile, as shown in Figure 3.c. Loading to yield sets the elastic stress, whereas unloading removes the elastic stress. Because unloading does not change the electrochemical potential, it is assumed that the elastic stress has no influence on the thermodynamics of the electrode. The measurement was repeated 24 h after unloading, and the potential above all the surfaces increased by 10-20 mV (Figure 3.d).

The stress and stain distributions in the sample were modeled using the same deformation of 3%. The plastic strain profile is shown in Figure 3.a. The plastic strain was mainly concentrated at the center of the sample in the gauge section but also spread out from this area. At this elongation, plastic strain existed up to 10 mm from the center of the sample with a steep gradient moving outwards from the gauge section.

A higher load (2.7 kN – 540 MPa) was applied to a tensile sample, reaching a deformation of 20% in the gauge section, and the potential distribution presented in Figure 4 shows that the length of the stress-affected area was approximately 35 mm. A similar length was determined using the model presented in Figure 2.c. The initial potential profile was constant at 0.38 V vs. SHE, and due to the strain, the central area and the edges of the affected zone were characterized by lower potentials of 0.2 - 0.16 V vs. SHE. Thus, the plastic deformation decreased the potential of AISI 304 steel by about 180-220 mV, which is in agreement with the effect reported for 301LN stainless steel [25, 29].

The profile presented in Figure 4.b was measured after unloading and exposure to ambient air. The potential in the gauge section increased to 0.32 V vs. SHE and corresponded to the presence of residual stress, which can be ascribed to the dislocation field. Thus, it is possible to conclude that plastic deformation initially decreased the potential and then subsequently

increased the potential. It can be assumed that the decrease in the potential was linked to the emergence of new strain-induced surfaces (dislocations) [25, 29]. The increase in potential was related to the passivation of the newly formed metallic surfaces.

The impact of the tensile stress on the potential in the center of the gauge section was measured as a function of the load (Figures 5 and 6). At 220 MPa, corresponding to 0.33 % of strain, in the elastic domain, no effect of the load on the potential was observed. However, further increasing the load in the plastic deformation domain proportionally decreased the *in situ* potential of the surface measured under loading (Figures 5.a, c and Figure 6.a). The potential in Figures 5.a, c varies over a range from 7 to 10 mV, which is close to the noise level. Thus, the potential was relatively uniformly distributed without forming any ordered structures (taking into account a spatial resolution limit of 70-100 μm for the SKP instrument). However, the plastic stress creates dislocations that increase the surface roughness Figures 5.b, d (Table 2).

The graph presented in Figure 6.a shows that at lower loads, the potential decreased proportionally with the strain, and for larger elongations, the potential approaches a limit value of approximately 0.14 V vs. SHE. The graph contains the data for the maximal and minimal potentials measured in each map. After the profile measurements (Figure 5), the SKP tip was positioned above the surface to monitor possible changes in the potential (Figure 6.b). The evolution of the potential over 1000 s under a constant applied load shows that the= potential slowly increased during exposure in air, which can be ascribed to the passivation of= the newly formed surface.

The passivation process in air at 60% RH for a pre-strained sample was monitored for a longer period of time (*i.e.*, 19 h, as shown in Figure 7). The potential variations were modeled using a regression function, $\varphi = A \log(t) + const$, which can mimic equation 1 related time-dependent growth of the oxide film**.** In Figure 7, regression line 2 shows that the experimental dependence can be described by a logarithmic function. Coefficient A relates to the rate of passivation, and R is a regression coefficient (Table 3). A small amount of strain shows a low rate of passivation that then increases for higher loads. The probe is localized above a surface containing unaffected passive areas and the newly formed low-potential surfaces of the emerged dislocations. At low loads, the potential is averaged over the active and passive locations. At high loads, all the surfaces in the gauge section are relatively active. In this case, the probe monitors the passivation kinetics, which is nearly logarithmic (Table 3). Thus, the coefficient A depends on the ratio of active to passive surfaces, whereas the rate of passivation for a single dislocation must be determined using high spatial resolution electrochemical measurements.

To evaluate the effect of the elastic stress, the SKP maps were measured for the pre-strained gauge section (20% straining) under loading and load-free conditions (Figure 8.a, b). Unloading does not change the potential. This is in agreement with results obtained for low strains (Figure 3.b, c). Thus, it can be assumed that the potential of the strained surface is mainly determined by the density of the emerging dislocations and by their passivation due to coming into contact with air.

These results show that the emerged dislocations could be passivated either under an applied load or at the rest condition. The elastic stress has no influence on the potential of the plastically strained surface. However, it can increase the distance between surface atoms, which will affect the surface reactivity, *i.e.*, on the oxygen adsorption and the formation of the surface oxide film. Thus, it is important to compare the rates of passivation and the reactivity of the strained surfaces under loading and at rest. To determine the effect of loading

on the rate of passivation, the tensile sample was strained at 20%. Figure 9.a shows the monitored potential in the center of the gauge section after application of the strain (1st cycle). After 2400 s, the sample was unloaded, and the potential was monitored at the same location (unloaded, 2nd cycle). Figure 9.a shows that the curves of the first and the second cycles are parallel, indicating similar rates of steel passivation under the elastic stress and at rest. Figure 9.b compares the passivation curves obtained from two different samples after straining up to 20% in the gauge section. In one sample, the potential was monitored under loading, and in the second sample, the potential was monitored at rest. Both curves approach the potential measured before the stress was applied (Figure 9.b, curve 1). The experimental results show similar rates of passivation without significant influence from the applied elastic stress.

The surface of AISI 304 was pre-ground by using 4000 grit emery paper and then rinsed in ethanol. The potential above the steel was monitored 5 min after the surface treatment. Figure 10 compares the transient potentials after grinding and after straining at 15%. For the prestrained surface, potential monitoring was carried out under load-free conditions. Grinding produced a small amount of compressive stress without the emergence of dislocations [16]. In the case of plastic deformation, dislocations participate in passivation, and the potential was mainly determined by the dislocation density. The potential monitoring (Figure 10) shows the qualitative similarity of steel surface passivation after either straining or grinding.

### *3.2 Straining of an AISI 304 tensile sample in an aqueous electrolyte*

The effect of tensile stress on the OCP was measured by a saturated calomel reference electrode in an aqueous 0.5 M $Na_2SO_4$ electrolyte. For this purpose, a small electrochemical cell was attached to the gauge section of a tensile sample using a rubber O-ring. Figure 11 shows the OCP response after straining at 10% of plastic strain. The application of stress decreased the OCP by 150-200 mV, and then the potential increased due to passivation of the newly formed surfaces. The same sample was strained by an additional 10% of plastic strain, and a similar decrease in the OCP was obtained, followed by a slow increase. Thus, the influence of plastic deformation on the potential in an aqueous electrolyte compared favorably to the SKP results obtained in air (Figure 7, 10). Another sample was directly strained at 20% of plastic strain, and the passivation was monitored, as illustrated in Figure 11.b. The resulting passivation curve in the electrolyte could be fit with a logarithmic regression with a coefficient *A* equal to 0.03 (Table 3). The passivation curve in an aqueous electrolyte was also measured after grinding a steel electrode, which gave a similar passivation curve. Thus, the effects of stress on surface activation and subsequent passivation in an aqueous electrolyte are similar to those observed under ambient air conditions. These data are in agreement with previously reported OCP measurements performed on AISI 305 steel in a NaCl electrolyte [18].

### *3.3 SECM study of the passivation of AISI 304 steel*

The effect of the tensile strain on the local electrochemical reactivity was studied in the same 0.5 M $Na_2SO_4$ aqueous electrolyte. SECM was used to assess the passivation of the emerging dislocations under loading (Figure 12).

Figure 13 shows the logarithmic scale time dependencies for the mediator reduction currents (measured at the open circuit potential). The rates of passivation (slopes of the straight lines) are the same for strains of 5% and 8%. On the other hand, an increase in the strain is

accompanied by an increase in the tip current, which was attributed to an increase in the density of dislocations emerging from the surface. Thus, the rate of passivation as a function of the plastic deformation can be determined. These results show that after the application of a plastic deformation, the steel becomes more active (from an electrochemical point of view), and passivation upon exposure to air or in an inert aqueous electrolyte is a relatively long-term process.

### *3.4 SKP and SECM studies of surfaces containing residual stress.*

Plastic deformation often occurs during the production of steel. The deformation results in a high defect density in the matrix, resulting in a less protective passive film [18, 22]. Thus, it was reasonable to use SKP and SECM to study the surface of AISI 304 samples containing residual stress. Figure 14.a shows the potential profile after applying 20% elongation using a tensile machine followed by exposure to dry air for two weeks. We assumed that after this time, the surface of the steel sample was close to the steady-state conditions. The left side of the sample was under elastic stress and thus has no additional dislocations and can be considered a reference. The right side of the samples was plastically deformed (Figure 14.a). The gauge section (right side) showed a potential that was 30-40 mV lower than that of the reference side.

The same sample was slightly ground using 4000 grit emery paper, rinsed and then exposed to dry air for 2 weeks. The potential map presented in Figure 14.b shows that the substrate containing residual stress (dislocations) was covered by an oxide film with a low potential. Thus, a surface containing dislocations is able to re-passivate, but the oxide film shows different properties than those of the reference material (*i.e.*, the sample without residual stress). This can be explained as a result of an increase in the density of defects and changes in either the conducting properties of the oxide film, its thickness or its composition. In fact, grinding can add additional compressive or shear stress [16]. It can complicate the final distribution of residual stress and potential. Thus, more studies in this field is required.

After pre-straining the samples at different levels using a straining technique (see the Experimental Section), they were exposed to dry air in a desiccator to stabilize the potential and passivate the surface. The surfaces were then characterized by SECM and SKP to evaluate the changes in their surface reactivity (Figure 15). SECM was performed using ferrocene methanol as a redox mediator in an aqueous $Na_2SO_4$ (0.5 M) electrolyte to study the reactivity of the surfaces as a function of the strain. The current variations (Figures 15.c and e) indicate that the reactivity of the surfaces increase with increasing levels of applied strain and, correspondingly, with increasing amounts of dislocations and residual stress. Additionally, the SECM images show that even if the overall reactivity increases with increasing loads, the reactivity is no longer homogeneous for loads corresponding to 20% and 30% deformations.

The SECM data are in good agreement with the SKP results (Figure 15.d, f), in which island-like structures were also found. However, the differences in potential are relatively small (10-20 mV). It can be supposed that the island-like structures are the result of variations in the properties of the surface oxide film (thickness, composition, electron-hole density and conductivity) near the dislocations.

### *3.5 XPS study of the influence of strain on the passive film*

XPS spectra were obtained for unstrained sample and a sample after 20% elongation. The time between applying the strain and the XPS measurements was rather long; thus, repassivation of the surface had occurred. Using the model for a $Cr_2O_3/Fe_2O_3$ bilayer, the total thickness of the passive layer on the unstrained sample was estimated to be 1.65 nm, with 0.64 +/- 0.13 nm of Cr oxide and 1.01 +/- 0.14 nm of Fe oxide. After straining, a slightly thicker layer was obtained, with a total thickness of 1.87 nm, corresponding to 0.65 +/- 0.14 nm of Cr oxide and 1.22 +/- 0.04 nm of Fe oxide. These measurements are in agreement with literature data, which indicate a thickness of the passive film in the range of 1.5-2 nm for a 304L alloy [34].

The oxygen in the sample was also investigated, and the relative amount of $-O_2$ and -OH bonding was estimated using peak deconvolution. A representative example of the deconvolution is given in Figure 16 for the unstrained sample analyzed at 0°. The concentration was estimated using the area of each peak.

The results are shown in Figure 17. With increasing analysis angle, which results in an analysis closer to the top surface, the contribution of -OH increased for both the unstrained and strained samples. Thus, the top layer was most likely enriched with iron hydroxides, such as FeOOH. Interestingly, the contribution of -OH was systematically higher for the strained sample and rather stable with respect to analysis angle. The increased amount of -OH groups close to the interface in the pre-strained steel sample can result from the formation of a less dense oxide film. XPS analysis showed that the composition of the passive layer was affected by the plastic deformation, without a strong influence on the thickness of the passive layer.

## 4. Discussion

It is important to discuss the links between the potential measured by the SKP technique and the properties of the steel surface that influence mechanical activation. Equation 3 shows that the measured potential is proportional to the potential drop of the passive oxide film. According to the work of N. Sato, the potentials of different metals are proportional to the thickness of their oxide film [35]. For example, a linear dependence was experimentally determined for different alloys (e.g., Fe-Ni alloy) over a range of potentials related to the passivity [36]. Equation 4 shows the link between the potential of a passive metal ($\varphi_M$) and the corresponding oxide thickness and dielectric constant:

$$\varphi_H = \varphi_M \left(1 + \frac{L}{\partial} \frac{\mathcal{E}_H}{\mathcal{E}_{ox}}\right)^{-1} \qquad \text{(Eq. 4)},$$

where $\varphi_H$ is the potential drop across the Helmholtz layer of the electrolyte, $\varphi_M$ is the overall potential drop of the metal-solution interface, L is the thickness of the oxide film, $\partial$ is the thickness of the Helmholtz layer, and $\mathcal{E}_{ox}$ and $\mathcal{E}_H$ are the dielectric constants of the film and of the Helmholtz layer, respectively [35]. The linear dependence between the SKP-measured potential and the thickness of the oxide film that grows after grinding of 301LN stainless steel was determined by SKP in a previous report [29]. XPS shows that the plastic strain does not significantly influence the composition and thickness of the surface oxide, and we can assume that the measured potential is proportional to the oxide film thickness.

In this study, SKP and SECM techniques were shown to be able to determine the effects of the stress on the local electrochemical properties of the steel electrode. SKP was able to

characterize the level of passivity of the AISI 304 steel surface as a function of the strain. Because plastic deformation creates dislocations (Figure 5) that cross the initial oxide film, the decrease in the potential was explained by the formation of new surfaces. Indeed, the emergence of dislocations increases the surface roughness and the real surface area of the electrode (Table 2). The distribution of the local strain in the gauge section corresponds to the distribution of the potential (Figures 3 and 4). Thus, we can assume that a potential decrease corresponds to the dislocation density and depends on the applied stress. Figure 6.a shows that for a low strain, the potential proportionally decreases, and at higher elongations, the potential approaches the minimum steady-state value. This is in agreement with the effect of the strain on the dislocation density [37]. Thus, at low strains, the density of dislocations proportionally increases, but at high strain, the density is stable due to the interaction and annihilation of dislocations [37]. The elastic stress does not create dislocations and has no influence on either the initial potential of the steel surface or the potential of a surface containing dislocations.

SKP measurements started approximately 5 min after the application of stress. The potential increased due to passivation of the new surfaces. Extrapolation of the time-dependence curves (e.g., Figures 7 and 9) to the initial time show that the initial potential is more positive than the either reversible potential of oxide formation or the flat band potential of the oxide film (-0.3 V vs. SHE at pH 9.2) [20, 38]. Thus, rapid oxygen adsorption at the active dislocations and formation of the first layers of the oxide could not have been studied with the approach used here. The time dependence of the potential follows a logarithmic regression curve (Figure 7, Table 3). Deviation of the potential (Figure 7) from the basic logarithmic dependence was mainly observed at the beginning of the passivation process. Exposure to air of the pre-ground surface also increased the potential due to passivation (Figure 10). It is possible that the passivation kinetics can be described by the high-field Mot-Cabrera model for oxide film growth, whereas surface grinding may mimic the formation of new surfaces due to strain.

Plastic deformation creates “active” surfaces that accelerate the electron transfer and efficiency of the cathodic reduction of the oxidizer (mediator) in the SECM experiments. Due to surface passivation, the reduction currents decreased during exposure to the electrolyte (Figure 13). However, this process takes a relatively long time. These findings are in agreement with the study of G.T. Burstein [39], which determined that newly formed surfaces accelerate the water reduction and hydrogen evolution reactions. The subsequent decay of the cathodic current over time is relatively small, and the new surfaces remain catalytically active towards hydrogen evolution [39]. The SKP measurements in air correspond to the OCP measurements in a passivating aqueous electrolyte using a reversible reference electrode (Figure 11). Transient of OCP also show that passivation of a strained surface takes a long time. The difference in potentials between the stressed and stress-free areas promotes galvanic corrosion of the anodic locations that contain residual stress.

Different studies have interpreted the stress-induced acceleration of corrosion and anodic dissolution from the point of view of the mechano-electrochemical effect introduced by E. Gutman [8, 9]. This theory explains the acceleration of anodic dissolution from a thermodynamic perspective. The equilibrium potential of the metal is more negative than $\Delta\varphi$ (in volts) for an excess external pressure ($\Delta P$):

$$\Delta\varphi = -\frac{\Delta PV}{zF} \qquad \text{(Eq. 5)},$$

where V is the molar volume of the metal, z is the valence of the metal ion, and F is the Faraday constant. Thus, an increase in the external pressure ($\Delta P > 0$) accelerates the metal

dissolution rate. However, thermodynamic analysis [40] showed that the change in free energy due to elastic deformation is insufficient to significantly alter the active dissolution rate. Moreover, SKP measurements of the effect of the elastic tensile stress do not show a shift in the electrochemical potential of the AISI 304 electrode (Figures 3 and 8). However, it is worth to note that the effect was studied for well passivating alloy and in passive conditions. Perhaps this point cannot be directly applicable to systems corroding under activation control.

For the stress corrosion cracking mechanism, the important question concerns the impact of the elastic stress on the kinetics of passivation and the general reactivity of the strained surface. Figure 9 shows that the kinetics of oxide growth either under loading or at rest are similar. However, the properties of the oxide films formed under different conditions, such as film homogeneity and composition, were not determined in particular work.
Internal stress created by cold work changes the corrosion properties of metal surfaces. The steel incorporates the internal stress and back stress due to the interaction of the dislocations with the grain boundaries [22, 24]. Concerning the oxide film, the deformation increases the doped charge density (concentration of donors and acceptors) in the passive films of stainless steels [18-20, 41]. For pure iron, dislocations exposed to the iron surface increase the number of donors, resulting in a highly defective passive film [42]. In this particular study, after tensile straining and repassivation, SKP showed that the surface of the AISI 304 steel did not return to the initial level of passivity and that the potential was 30 mV lower than that of the unstrained reference area (Figure 14.a). It is important to note that, after removing the oxide film by grinding, repassivation creates a new oxide film that exhibits a lower potential drop in the regions with residual stress (Figure 14.b). Figure 15 shows that residual stress creates macroscale areas with non-uniform distributions of the potential and SECM current. In general, the electron transfer rate across the strained areas is higher relative to that of the initial reference surface (Figure 15). Thus, residual stress due to the formation of a dislocation field modifies the oxide film and increases the surface reactivity, which shows localization on the microscale.

## 4. Conclusions:

1. The effect of tensile stress on the electrochemical potential of 304 stainless steel was studied in air using SKP. The effect of elastic stress on the electrochemical potential of the steel electrode was not found. The plastic stress decreased the potential of the AISI 304 steel by 150-200 mV. This was ascribed to breaks in the passive film due to the emergence of dislocations and the formation of new active surfaces.

2. After passivity breakdown, the potential increases due to the formation of a new oxide film and passivation. The growth of the oxide layer is a long-term process. Stabilization of the potential proceeds after 24 h of exposure to air. The elastic tensile stress does not influence the rate of passivation. During passivation, the potential showed a logarithmic dependence that may be the result of oxide growth according the field assisted ion migration mechanism.

3. Monitoring of the open circuit potential after plastic deformation in an aqueous electrolyte showed that the passivation rate is similar to that measured in air. SECM was shown to be an efficient method for monitoring the passivation in an electrolyte as a function of the level of applied tensile strain. Newly formed surfaces showed long-term activity and an increased rate of electron transfer across the growing oxide film. Thus, long-term galvanic couples consisting of anodic ruptured areas and the surrounding cathodic surfaces will lead to corrosion at the stress location.

4. After passivation, the locations containing internal tensile stress show a lower potential relative to that of the reference surface due to the formation of more defects in the oxide film. The areas containing residual stress show a non-uniform potential distribution and accelerated electron transfer across the oxide film, which can lead to the development of local corrosion. XPS studies show that oxide films formed on plastically deformed steel have a less dense structure and an increased density of hydroxide groups than those of other oxide films.

## 5. References


1. S.F. Bubar and D.A. Vermilyea, Deformation of Passive Films, *J. Electrochem. Soc.,* **114,** 882 (1967).
2. R.M. Latanision and R.W. Staehle, Plastic deformation of electrochemically polarized nickel single crystals. *Acta Metall*., **17**, 307 (1969).
3. J.C. Scully, The Interaction of strain-rate and repassivation rate in stress corrosion crack propagation, *Corrosion Science*, **20,** 997 (1980).
4. J.R. Galvele, R.M. Torres and R.M. Carranza, Passivity breakdown, its relation to pitting and stress corrosion cracking processes, *Corrosion Science,* **31,** 563 (1990).
5. D.A. Vermilia, A Theory for the Propagation of Stress Corrosion Cracks in Metals- Technical Paper. *J. Electrochem. Soc.*, **119,** 405 (1972).
6. W.R. Wearmouth, G.P. Dean and R.N Parkins, Role of Stress in the Stress Corrosion Cracking of a Mg-Al Alloy, *Corrosion,* **29,** 251 (1973).
7. A.R. Despic, R.G. Raicheff and J. O'M Bockris, Mechanism of the Acceleration of the Electrodic Dissolution of Metals during Yielding under Stress, *The Journal of Chemical Physics*, **48**, 926 (1968).
8. E.M. Gutman, G. Solovioff and D. Eliezer, The mechanochemical behavior of type 316L stainless steel, *Corrosion Science,* **38,** 1141 (1996).
9. E.M. Gutman, Mechanochemistry of Materials, p.31, Cambridge, Interscience Publishing, Cambridge, (1998).
10. M. Sahal, J.Creus, R.Sabot ansd X. Feaugas, The effects of dislocation patterns on the dissolution process of polycrystalline nickel, *Acta Materialia,* **54**, 2157 (2006).
11. K. Saito and J. Kuniya, Mechanochemical model to predict stress corrosion crack growth of stainless steel in high temperature water, *Corrosion Science*, **43,** 1751 (2001).
12. D. Large, R. Sabot and X. Feaugas, Influence of stress–strain field on the dissolution process of polycrystalline nickel in $H_2SO_4$ solution: An original *in situ* method, *Electrochimica Acta*, **52**, 7746 (2007).
13. G.T. Burstein and P.I. Marshall, Growth of passivating films on scratched 304L stainless steel in alkaline solution, *Corrosion Science*, **23**, 125 (1983).
14. R.M. Carranza, , J.R. Galvele, Repassivation kinetics in stress corrosion cracking-I. Type AISI 304 stainless steel in chloride solutions, *Corrosion Science*, **28,** 233 (1988).
15. B. MacDougall and M.J. Graham" Growth and Stability of Passive Films" in book *Corrosion Mechanisms in Theory and Practice,* 2nd edition, Ed. P. Marcus, p. 200, Marcel Dekker, Inc. New York Basel, (2002).
16. V. Vignal, C. Valot, R. Oltra, M. Verneau and L. Coudreuse, Analogy between the effects of a mechanical and chemical perturbation on the conductivity of passive films, *Corrosion Science,* **44** , 1477 (2002).

17. Y. Zhu, L. Li and C. Wang, Effects of tensile stresses on the oscillatory electro dissolution of X70 carbon steel in sulfuric acid solution, *Corrosion Science*, **94,** 445 (2015).
18. X. Feng, X. Lu, L. Guo and D. Chen, The Effects of Deformation on Corrosion Behaviour of Stainless Steel in Chlorides Contaminated Concrete Pore Solution, *Int. J. Electrochem. Sci.,* **10,** 10677 (2015).
19. L. Jinlong, L. Tongxiang, W. Chen and G. Ting, Effect of in site strain on passivated property of the 316L stainless steels, *Materials Science and Engineering, **C*** **61** 32 (2016).
20. C.M. Rangel, T.M. Silva and M. da Cunha Belo, Semiconductor electrochemistry approach to passivity and stress corrosion cracking susceptibility of stainless steels, *Electrochimica Acta*, **50,** 5076 (2005).
21. M. de O. Silva, H. Ferreira G. de Abreu, V. Hugo C de Albuquerque, P. de Lima Neto, J. Manual and R.S. Tavares, Cold deformation effect on the microstructures and mechanical properties of AISI 301LN and 316L stainless steels, *Materials and Design,* **32**, 605 (2011).
22. L. Peguet, B. Malki and B. Baroux, Influence of cold working on the pitting corrosion resistance of stainless steels, *Corrosion Science*, **49,** 933 (2007).
23. O. Takakuwa and H. Soyama, Effect of Residual Stress on the Corrosion Behavior of Austenitic Stainless Steel, *Advances in Chemical Engineering and Science,* **5,** 62 (2015).
24. Y. Boudinar, K. Belmokre, M. Touzet, O. Devos and M. Puiggali; The high frequency capacitance obtained by EIS: a good way to investigate the passivation process. Effect of plastic strain on a 316L, *Materials and Corrosion*, **70,** 206 (2019).
25. A. Nazarov, V. Vivier, D. Thierry, F. Vucko, and B. Tribollet, Effect of Mechanical Stress on the Properties of Steel Surfaces: Scanning Kelvin Probe and Local Electrochemical Impedance Study, *J. Electrochem. Soc.*, **164**, C66 (2017).
26. P. Sun, Z. Liu, H. Yu and M.V. Mirkin, Effect of Mechanical Stress on the Kinetics of Heterogeneous Electron Transfer, *Langmuir,* **24**, 9941(2008).
27. D. Sidane, O. Devos, M. Puiggali, M. Touzet, B. Tribollet and V. Vivier, *Electrochemistry Communications,* **13,** 1361(2011).
28. D. Sidane, M. Touzet, O. Devos, M. Puiggali, J.P. Larivière and J. Guitard, Investigation of the surface reactivity on a 304L tensile notched specimen using scanning electrochemical microscopy, *Corrosion Science,* **87**, 312 (2014).
29. N. Fuertes Casals, A. Nazarov, F. Vucko, R. Pettersson and D. Thierry, Influence of Mechanical Stress on the Potential Distribution on a 301 LN Stainless Steel Surface, *J. Electrochem. Soc.,* **162,** C465 (2015).
30. A. Nazarov and D. Thierry, Application of Volta potential mapping to determine metal surface defects, *Electrochimica Acta,* **52**, 7689 (2007).
31. R. Hausbrand, M. Stratmann and M. Rohwerder, The physical meaning of electrode potentials at metal surfaces and polymer/metal interfaces: Consequences for delamination, *J. Electrochem. Soc.,* **155,** C369 (2008).
32. M. Stratmann, The investigation of the corrosion properties of metals, covered with adsorbed electrolyte layers – A new experimental technique, *Corrosion Science,* **27,** 869 (1987).
33. P.J. Cumpson and M.J. Seah, Elastic Scattering Corrections in AES and XPS. II. Estimating Attenuation Lengths and Conditions Required for their Valid Use in Overlayer/Substrate Experiments, *Surface and Interface Analysis,* **25**, 430 (1997).

34. R.-H. Jung, H. Tsuchiya and S. Fujimoto, XPS characterization of passive films formed on Type 304 stainless steel in humid atmosphere, *Corrosion Science*, **58**, 62 (2012).
35. N. Sato and Go Okamoto, Electrochemical passivation of Metals, in book *Comprehensive Treatise of Electrochemistry*, Eds. J.O'M Bockris, B.E. Conway, E. Yeager, E.E. White, **4**, p. 228, Plenum Press, New York & London (1981).
36. M. Seo and N. Sato, In-depth profiles of anodic oxide films on Fe-Ni alloy in boric acid-sodium borate solutions, *Corrosion Science*, **18**, 577 (1978).
37. L. Kubin, B. Devincre and T. Hoc, The deformation stage II of face-centered cubic crystals: Fifty years of investigations, *Int. J. Mater. Res*., **100**, 1411 (2009).
38. N.B. Hakiki, S. Boudin, B. Rondot and M. Da Cunha Belo, The electronic structure of passive films formed on stainless steels, *Corrosion Science*, **37,** 1809 (1995).
39. G. T. Burstein, Accelerated Evolution of Hydrogen on Freshly Generated Metal Surfaces in Aqueous Solution, *J. Electrochem. Soc.*, **131**, 991 (1984).
40. B.T. Lu, J.L. Luo, P.R. Norton and H.Y. Ma, Effects of dissolved hydrogen and elastic and plastic deformation on active dissolution of pipeline steel in anaerobic groundwater of near-neutral pH, *Acta Mater.*, **57,** 41 (2009).
41. L.V. Jin-long and L. Hongyun, Electrochemical investigation of passive film in pre-deformation AISI 304 stainless steel, *Applied Surface Science*, **263**, 29 (2012).
42. Y. Yamamoto, K. Fushimi, S. Miura, H. Konno, Influence of substrate dislocation on passivation of pure iron in pH 8.4 borate buffer solution. *J. Electrochem. Soc*., **157**, C231 (2010).

*Table 1: Composition of the austenitic AISI 304L steel used in this study (wt. %).*

| C(%) | Si(%) | Mn(%) | P(%) | S(%) | Cr(%) | Ni(%) |
|---|---|---|---|---|---|---|
| Max 0.03 | 0.6 | 1.5 | Max 0.045 | Max 0.03 | 18.5 | 9.5 |

*Table 2: Data of the 3D-optical topography profiling for the samples with residual stress.*

| Sample | State pre-treatment | Roughness (Ra in nm) |
|---|---|---|
| Reference | Fine polishing (1µm) | 51 |
| 10% tensile | Fine polishing (1µm) + tensile strain at 10% | 840 |
| 30% tensile | Fine polishing (1µm) + tensile strain at 30% | 1680 |

*Table 3: Regression dependence ($\varphi$= A log (t) +const.) for steel passivation after stress, and the R-regression coefficient.*

| strain | A | R | |
|---|---|---|---|
| 0% | 0.033 | 0.97 | abraded electrode |
| 8% | 0.014 | 0.887 | under load |
| 10% | 0.03 | 0.965 | Under load in aqueous electrolyte |
| 15% | 0.023 | 0.97 | Under load |
| 20% | 0.036 | 0.946 | under load |
| 20% | 0.033 | 0.956 | unloaded |
| 30% | 0.036 | 0.95 | Under loaded |

**Captions of the Figures:**

*Figure 1: Microstructure of the AISI 304L alloy.*

*Figure 2: A schematic of the tensile samples (a), the relation between stress, load and strain (b) and the calculated plastic strain distribution in the gauge section for a displacement of 6 mm (c). Inset in Figure 2.b shows zoom for low strain part of the curve.*

*Figure 3: The potential distribution along the gauge section with a 3% elongation load. a, b- samples under loading, a- 20 min after application of stress, b - 5 h after application of stress, c - samples from (b) measured after unloading, d – after resting for 24 h after unloading. Additionally, the inset in (a) shows the potential distribution and modeled distribution of the plastic strain across the gauge section for 3% elongation.*

*Figure 4: Potential distribution across the gauge section under a 20% elongation strain (a) after unloading and (b) after unloading and 24 h of exposure in air.*

*Figure 5: Potential distributions (a, c) measured in the center of the gauge section after the application of stress and topography of the surfaces (b, d). a, b -12% elongation; c, d- 20% elongation. The potential was mapped under loading in air at 60% RH, and the topography was measured using an optical profilometer without an external load.*

*Figure 6: Effect of the plastic strain on the potential (a). Monitoring of the steel potential under different loads in air at 60% RH (b).*

*Figure 7: The potential monitored in the center of the tensile sample under load and applied strains of 8%, 15% and 20%. A logarithmic regression line fits the curve of 15% strain.*

*Figure 8: Potential measured by SKP of the pre-strained surface (20% deformation) under load (a) and at rest 0 kN (b). The measurements were carried out 5 h after application of the load.*

*Figure 9: Monitoring of the potential in the gauge section after application of a 20% strain. a- curves measured under the loaded and unloaded conditions with linear regression lines. b- Potential monitoring of two different samples. Curve 1 was measured before loading, curves 2 and 3 were measured after application of the plastic strain. The measurement was carried out under loading (curve 3) and at rest (curve 2).*

*Figure 10: Monitoring of the electrochemical potential for an unloaded tensile sample after straining (15% elongation) and for a sample after grinding (4000 grit emery paper).*

*Figure 11: Influence of the tensile strain on the OCP monitored after loading in an aqueous 0.5 M $Na_2 SO_4$ electrolyte. a- two cycles of 10% of plastic strain ($\varepsilon_p$); b- plastic strain of 20%.*

*Figure 12: SECM approach curves in 0.5 M $Na_2SO_4$ + 10 mM $K_3(Fe(CN)_6)$ measured at different times after the application of strain a- 5% and b- 8% .*

*Figure 13: The local currents for the reduction of the mediator 10 mM $K_3(Fe(CN)_6)$ vs. time of exposure to the electrolyte after the application of stress. The tensile sample was strained to 5% (curve 2) and 8% (curve 1) of the total strain.*

*Figure 14: Potential distribution across the sample surface with 20% elongation and exposure to dry air for 2 weeks (a) and the same sample after grinding and exposure to dry air for 2 weeks (b).*

*Figure 15: Maps of the distribution of the SECM current probe in a 0.5 M $Na_2SO_4$ electrolyte (a,c,e) and SKP maps (b, d, f) of the pre-strained samples a, b- 0%, c, d - 20% and e, f- 30% strain.*

*Figure 16: Example of a de-convoluted oxygen peak used to evaluate the contributions of O (~529.5 eV), -OH (~531.3 eV) and $H_2O$ (~532.8 eV).*

*Figure 17. Changes in the relative contributions of O and -OH bonds with changing of analysis angle for the unstrained (left) and strained (right) samples.*

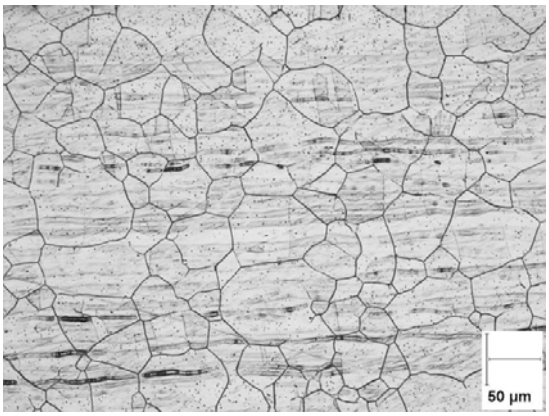


*Figure 1.*

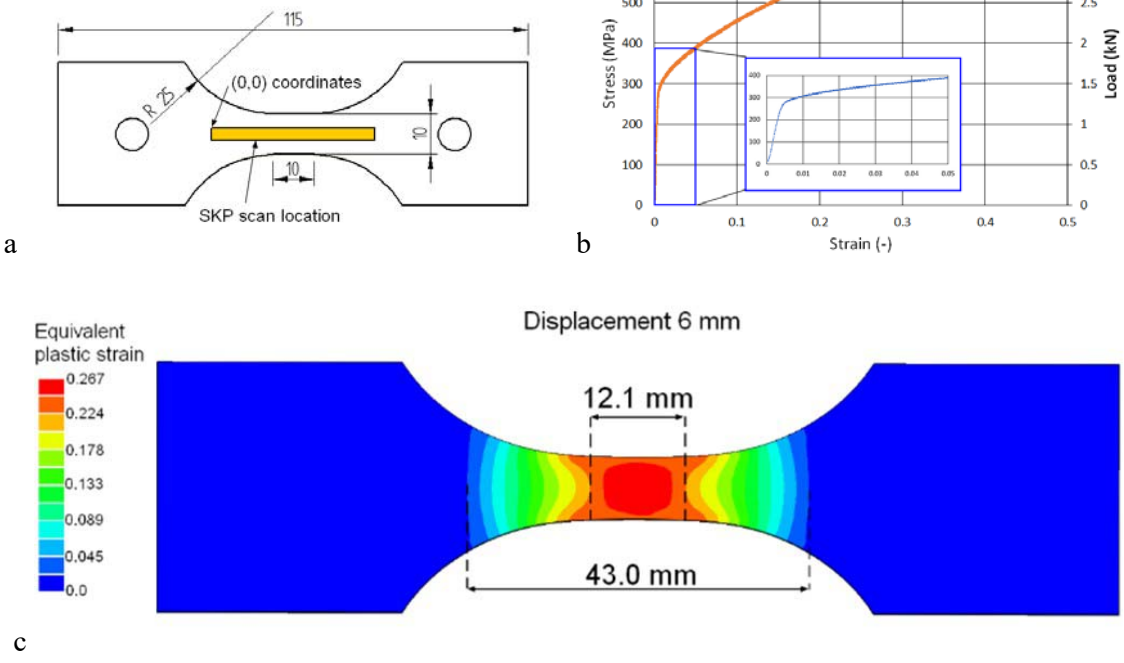
115
R 25
(0,0) coordinates
10
10
SKP scan location
a
700
600
500
400
300
200
100
0
Stress (MPa)
3.5
3
2.5
2
1.5
1
0.5
0
Load (kN)
0
0.1
0.2
0.3
0.4
0.5
Strain (-)
b
Equivalent plastic strain
0.267
0.224
0.178
0.133
0.089
0.045
0.0
Displacement 6 mm
12.1 mm
43.0 mm
c

*Figure 2.*

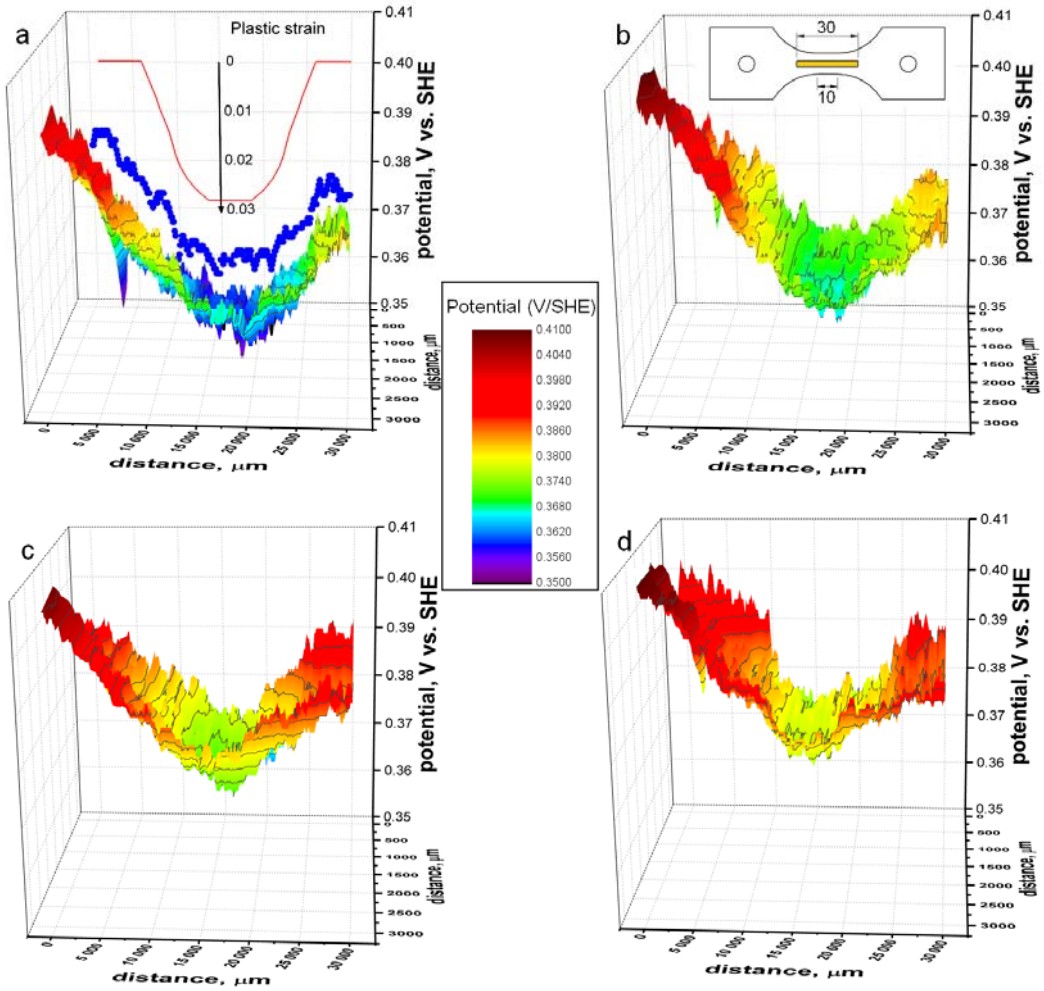
a
Plastic strain
0
0.01
0.02
0.03
potential, V vs. SHE
distance, μm
b
30
10
c
d
Potential (V/SHE)
0.4100
0.4040
0.3980
0.3920
0.3860
0.3800
0.3740
0.3680
0.3620
0.3560
0.3500

*Figure 3.*

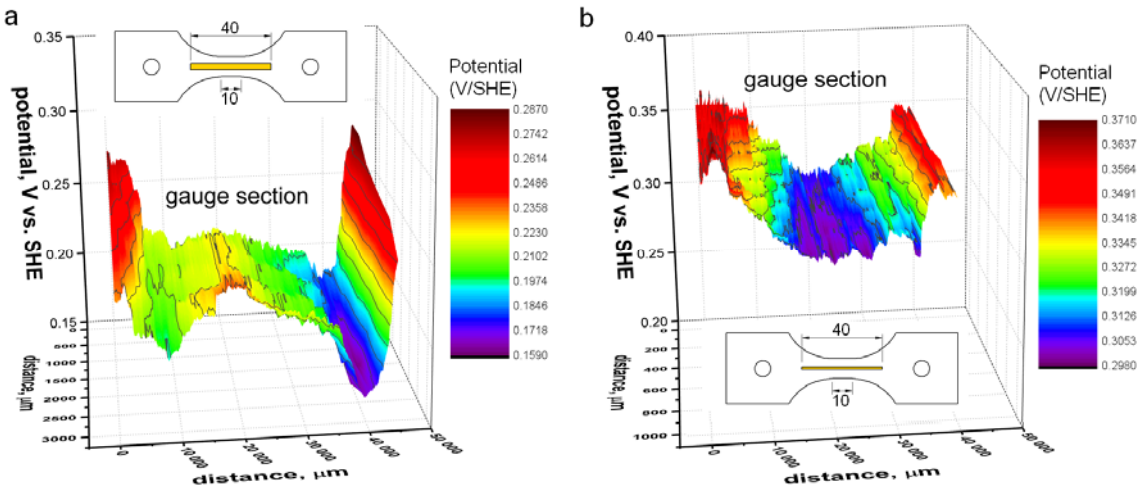
a
40
10
gauge section
potential, V vs. SHE
distance, µm
Potential
(V/SHE)
b
gauge section
potential, V vs. SHE
distance, µm
Potential
(V/SHE)

*Figure 4.*

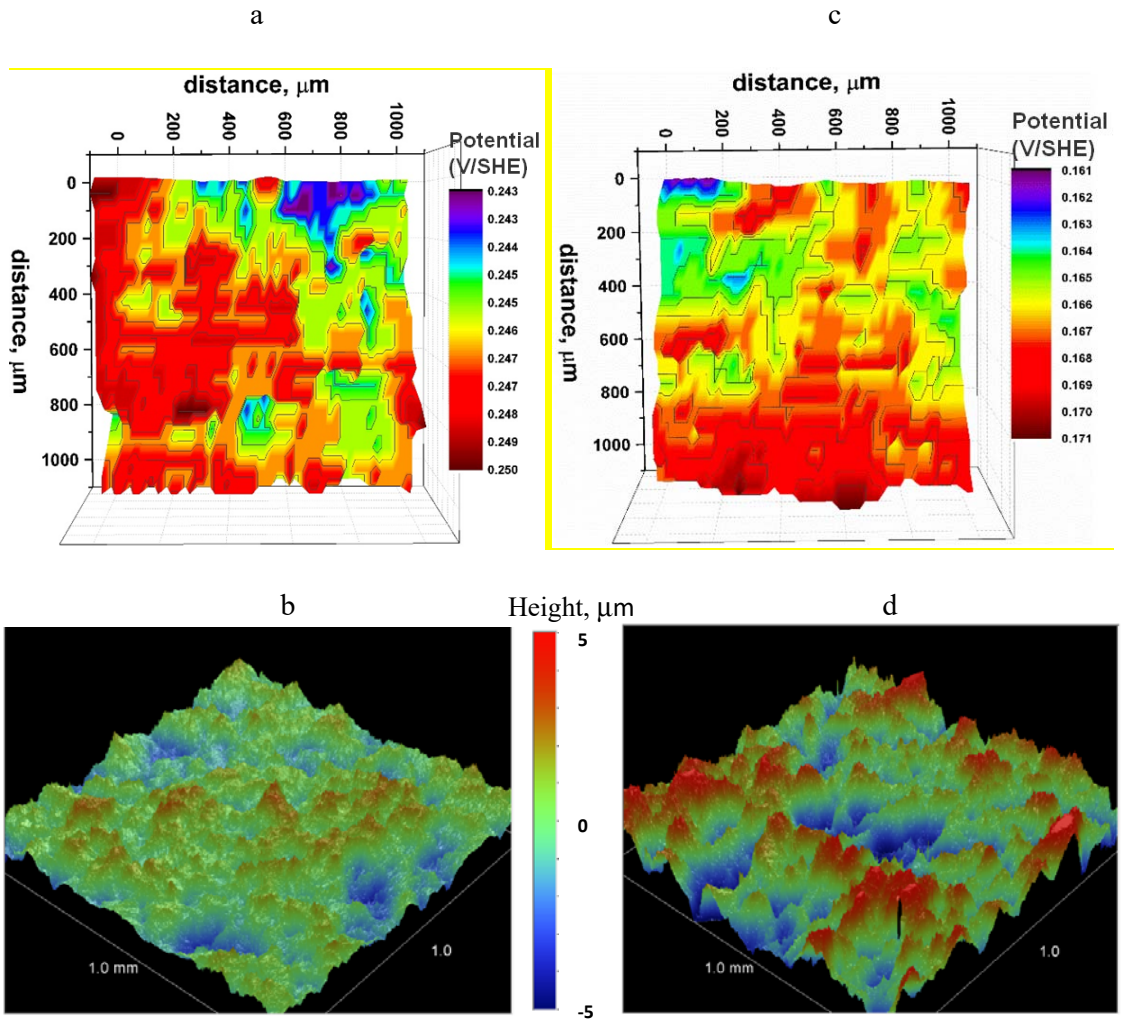
a
c
distance, µm
Potential (V/SHE)
distance, µm
b
Height, µm
d
1.0 mm
1.0

*Figure 5.*

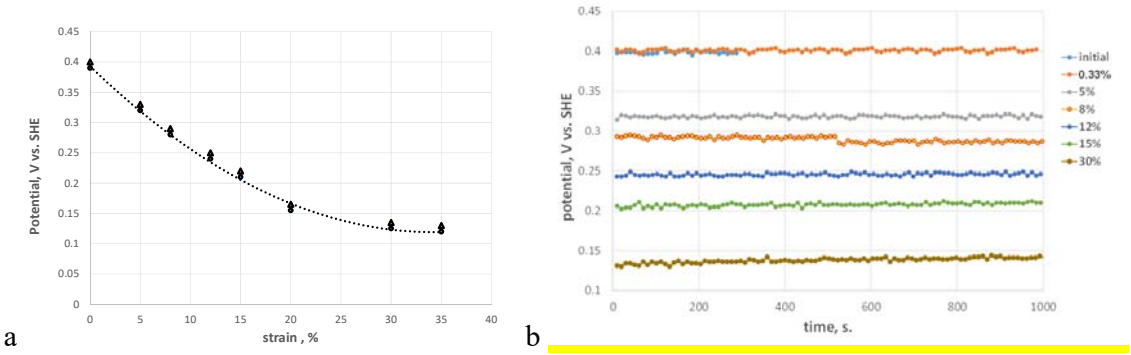


a b

*Figure 6.*

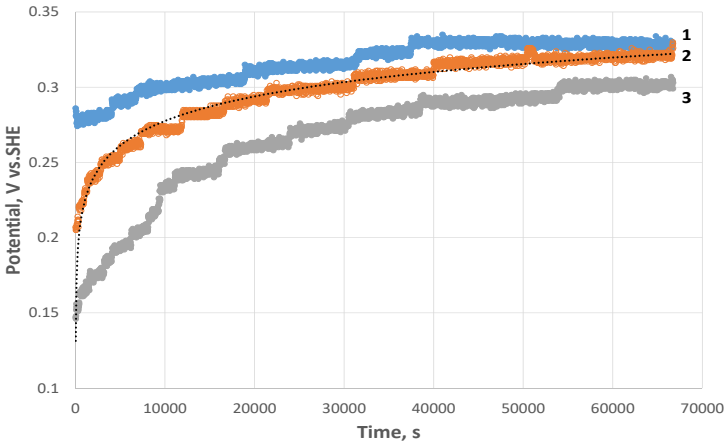


*Figure 7.*

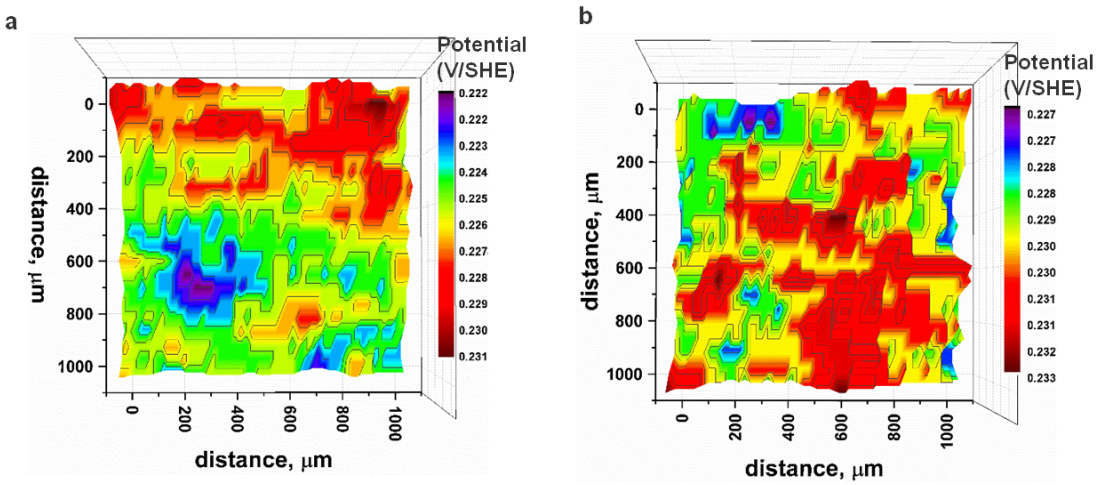


*Figure 8.*

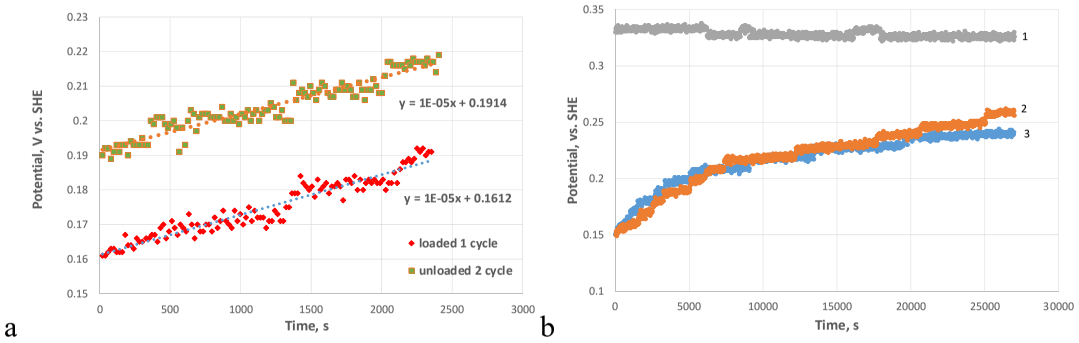


*Figure 9.*

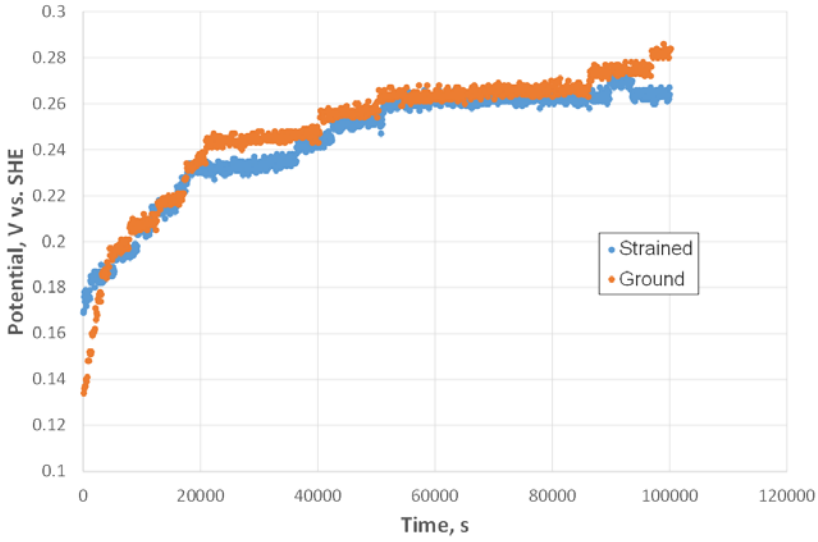


*Figure 10.*

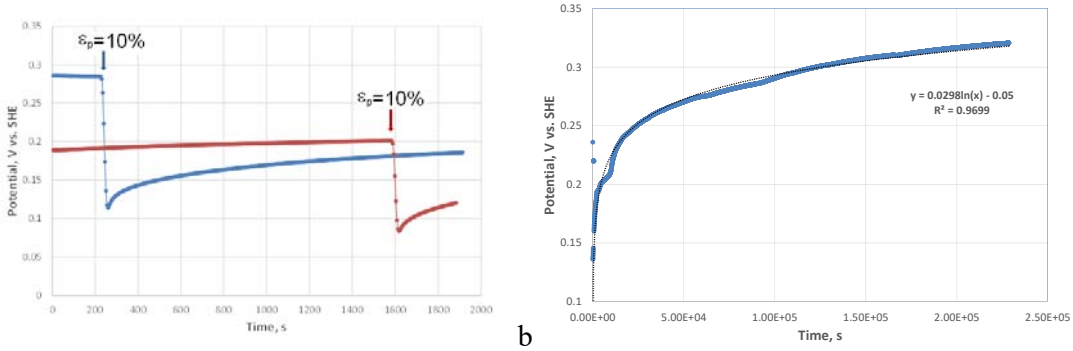


a b

*Figure 11.*

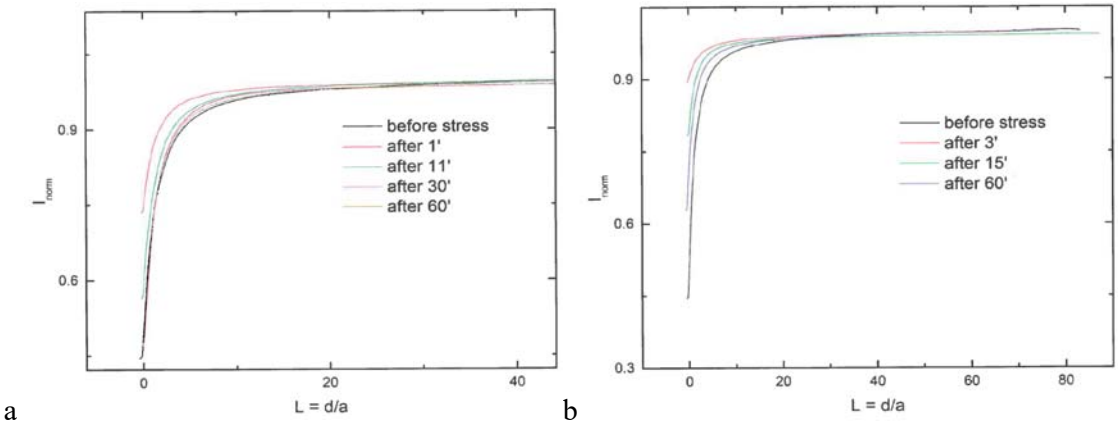


a b

*Figure 12.*

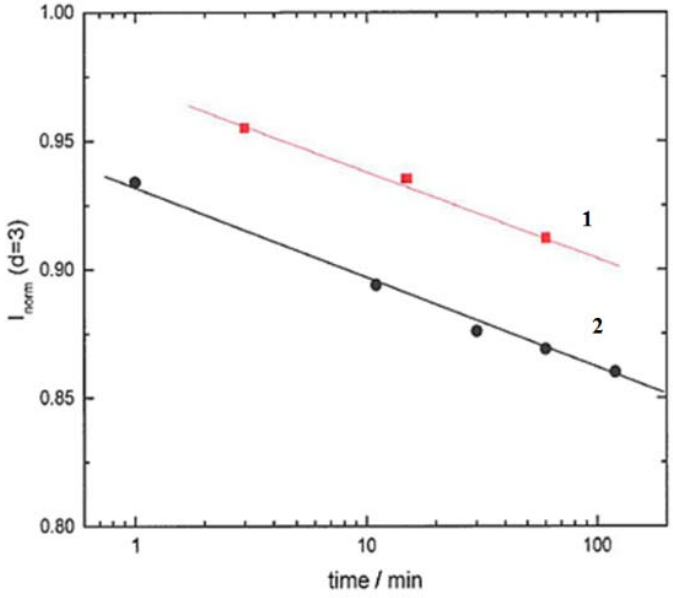


*Figure 13.*

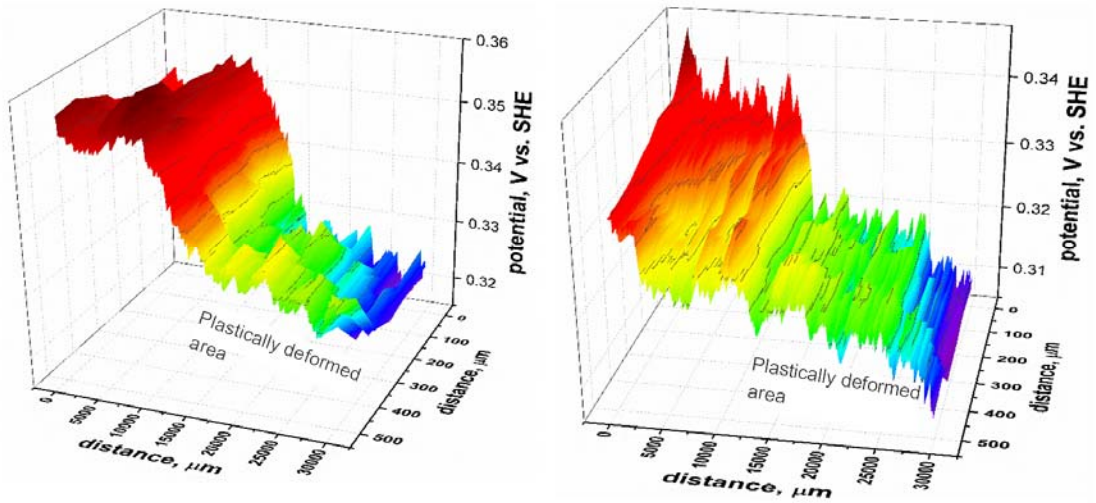
potential, V vs. SHE
0.36
0.35
0.34
0.33
0.32
Plastically deformed area
distance, µm
0
5000
10000
15000
20000
25000
30000
distance, µm
0
100
200
300
400
500
potential, V vs. SHE
0.34
0.33
0.32
0.31
Plastically deformed area
distance, µm
0
5000
10000
15000
20000
25000
30000
distance, µm
0
100
200
300
400
500

*Figure 14.*

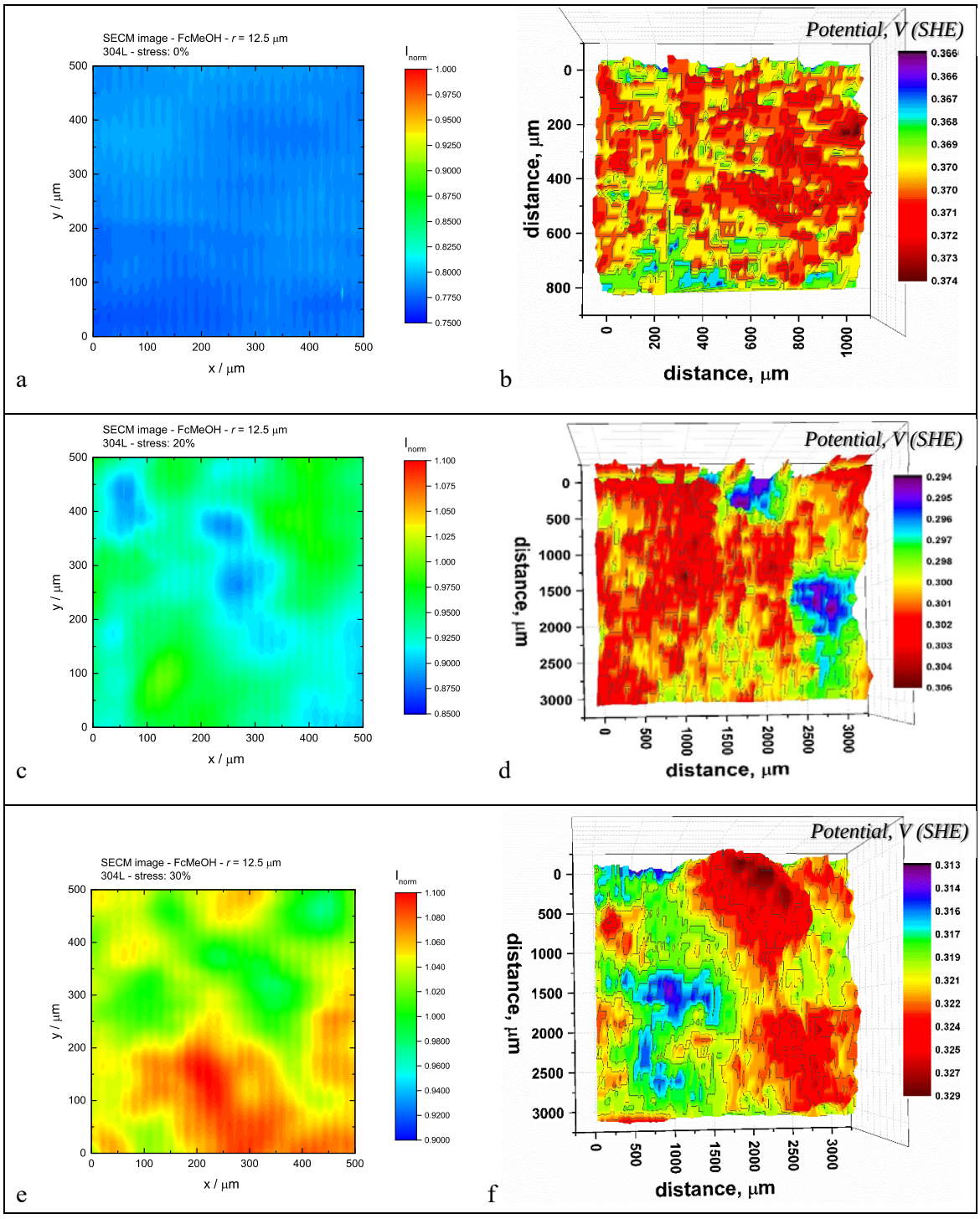
SECM image - FcMeOH - r = 12.5 µm
304L - stress: 0%
I norm
y / µm
x / µm
a
Potential, V (SHE)
distance, µm
distance, µm
b
SECM image - FcMeOH - r = 12.5 µm
304L - stress: 20%
I norm
y / µm
x / µm
c
Potential, V (SHE)
distance, µm
distance, µm
d
SECM image - FcMeOH - r = 12.5 µm
304L - stress: 30%
I norm
y / µm
x / µm
e
Potential, V (SHE)
distance, µm
distance, µm
f

*Figure 15.*

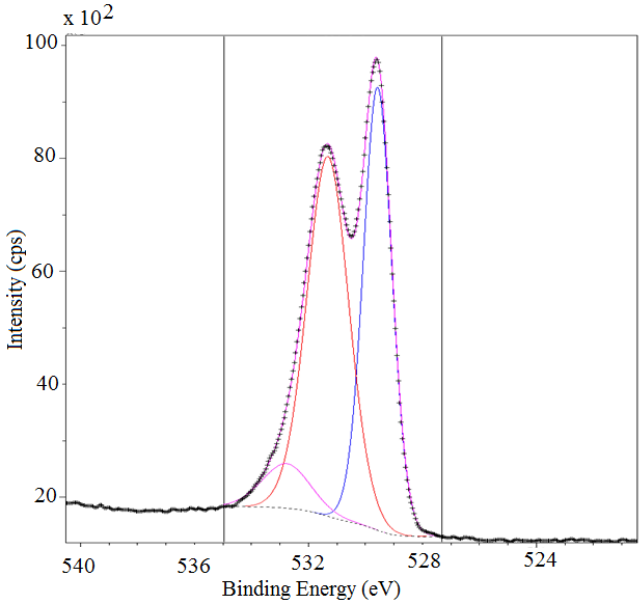


*Figure 16.*

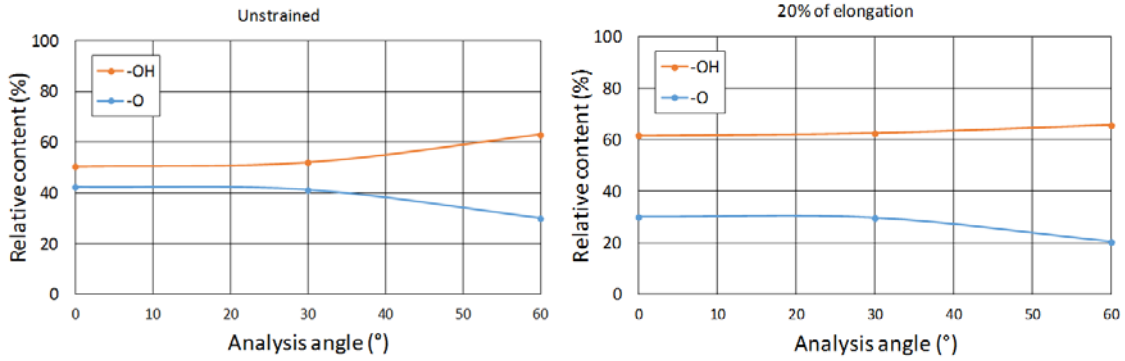


*Figure 17.*